

# Changing the Electronic Polarizability of Monolayer MoS<sub>2</sub> by Perylene-Based Seeding Promoters

Christian Martella, Erika Kozma, Pinaka Pani Tummala, Saverio Ricci, Kishan Ashokbhai Patel, Anita Andicsovà-Eckstein, Fabio Bertini, Guido Scavia, Roman Sordan, Luca G. Nobili, Monica Bollani, Umberto Giovanella, Alessio Lamperti,\* and Alessandro Molle

Large area molybdenum disulfide (MoS<sub>2</sub>) monolayers are typically obtained by using perylene-3,4,9,10-tetracarboxylic acid tetrapotassium salt (PTAS) as organic seeding promoter in chemical vapor deposition (CVD). However, the influence of the seeding promoter and the involvement of the functional groups attached to the seed molecules on the physical properties of the MoS<sub>2</sub> monolayer are rarely taken into account. Here, it is shown that MoS<sub>2</sub> monolayers exhibit remarkable differences in terms of the electronic polarizability by using two representative cases of seeding promoter, namely, the commercial PTAS and a home-made perylene-based molecule, *N,N*-bis-(5-guanidil-1-pentanoic acid)-perylene-3,4,9,10-tetracarboxylic acid diimide (PTARG). By thermogravimetric analysis, it is verified that the thermal degradation of the promoters occurs differently at the CVD working condition: with a single detachment of the functional groups for PTAS and with multiple thermal events for PTARG. As a consequence, the promoter-dependent electronic polarizability, derived by free charges trapped in the monolayer, impacts on the photoluminescence emission, as well as on the electrical performances of the monolayer channel in back-gated field-effect transistors. These findings suggest that the modification of the electronic polarizability, by varying the molecular promoter in a pre-growth stage, is a path to engineer the MoS<sub>2</sub> opto-electronic properties.

## 1. Introduction

Molybdenum disulfide (MoS<sub>2</sub>), a member of transition metal dichalcogenides (TMDs),<sup>[1]</sup> has emerged as outstanding 2D semiconducting material with potential applications in electronics, optoelectronics, valleytronics, catalysis, etc.<sup>[2–8]</sup> However, before harnessing the fascinating properties of monolayer MoS<sub>2</sub>, it is important to develop feasible fabrication methods extendable to large surface areas.<sup>[9,10]</sup> This is the first step toward the translation of 2D layered materials from laboratory scale to the industrial settings. In this respect, chemical vapor deposition (CVD) assisted by molecular seeding promoters represents the most promising way to control the kinetic of the growth, enabling the formation of 2D single-crystal domains rather than 3D cluster nucleation.<sup>[9,11]</sup>

The use of perylene-3,4,9,10-tetracarboxylic acid tetrapotassium salt (PTAS) is reported as a standard ingredient for the CVD growth of large area MoS<sub>2</sub> monolayer domain (up to 100 μm<sup>2</sup> scale otherwise

Dr. C. Martella, P. P. Tummala, Dr. A. Lamperti, Dr. A. Molle  
CNR-IMM

Unit of Agrate Brianza  
via C. Olivetti 2, Agrate Brianza, MB 20864, Italy  
E-mail: alessio.lamperti@mdm.imm.cnr.it

Dr. E. Kozma, Dr. F. Bertini, Dr. G. Scavia, Dr. U. Giovanella  
CNR-SCITEC

via A. Corti 12, Milano 20133, Italy

S. Ricci, Dr. K. A. Patel, Prof. R. Sordan  
L-NESS

Department of Physics  
Politecnico di Milano

Via Anzani 42, Como 22100, Italy

 The ORCID identification number(s) for the author(s) of this article can be found under <https://doi.org/10.1002/admi.202000791>.

Dr. A. Andicsovà-Eckstein

Polymer Institute

Slovak Academy of Sciences

Dúbravská cesta 9, Bratislava 84541, Slovakia

Prof. L. G. Nobili

Dipartimento di Chimica

Materiali e Ingegneria Chimica “Giulio Natta” Politecnico di Milano

Via Mancinelli 7, Milano 20131, Italy

Dr. M. Bollani

CNR-IFN

P.zza Leonardo da Vinci 32, Milano 20133, Italy

DOI: 10.1002/admi.202000791

unachievable in bare CVD process) as a result of the nucleation free-energy lowering.<sup>[11]</sup> Recent studies have shown the change in the physical properties of the MoS<sub>2</sub> monolayers using different seeding promoters.<sup>[12]</sup> Nevertheless, a clear understanding of the mechanism at the basis of the observed differences is still not comprehensively understood. To shed the light on these aspects, we investigated MoS<sub>2</sub> monolayers obtained using either the standard PTAS or a molecular engineered seeding promoter PTARG (*N,N*-bis-(5-guanidyl-1-pentanoic acid)-perylene-3,4,9,10-tetracarboxylic acid diimide). Both seeding molecules contain the extended perylene aromatic core, but the latter is enriched with different functional units (-CO, -COO, -NH, etc.) that have already demonstrated to influence the opto-electronic properties of a monolayer MoS<sub>2</sub> when deposited on its surface.<sup>[13]</sup>

In this paper, we study the electronic polarizability of the monolayers as the quantity governing the opto-electronic properties at the 2D level, as well as the dielectric constant in the 3D case. Based on the electrostatic force microscopy (EFM) measurements, we found that the electronic polarizability, in the static regime, shows a promoter-dependent behavior. To understand the origin of this polarizability variation, we track the detachment of the functional groups of the promoters by using thermogravimetric (TGA) analysis. We demonstrated that, at high temperatures, the functional groups of PTAS and PTARG attached to the perylene core are lost and the perylene core is the only structure that remains intact after the heating process. Still, the detachment of the functional groups occurs in a single thermal event for PTAS and by multiple thermal events for PTARG. Accordingly, under CVD working conditions, the presence of the perylene core generates similar morphological properties for both seed-assisted MoS<sub>2</sub> monolayers, while the change in the electronic polarizability is influenced by the different degradation processes of the promoters. The change of the electronic polarizability is reflected in observable variation of the opto-electronic properties. One example comes from the different radiative recombinations of the exciton and trion population deduced from the photoluminescence (PL) spectra. A second example relies on the different trans-characteristics of field effect transistors (FETs) incorporating MoS<sub>2</sub> single layer channel treated with the two different growth promoters. Our findings suggest that molecular engineering of the seeding promoters may represent a viable tool in view of tailoring the physical properties of the MoS<sub>2</sub> monolayers for the development of nanoelectronic and photonic devices.<sup>[14–16]</sup>

In the following section, we discuss the investigation carried out on the samples by means of Raman scattering and X-ray photoelectron spectroscopy (XPS). In particular, we compare the core levels and valence band edges of the CVD grown MoS<sub>2</sub> with those of commercially available geological flakes in **Figure 1**. TGA is shown in **Figure 2** to determine the different degradation paths of the two organic seeding promoters in use during the CVD process. Eventually, we specialize our study on MoS<sub>2</sub> monolayer using EFM, PL spectroscopy, and the electrical characterization of FETs in **Figure 2** and **Figure 3**.

## 2. Results and Discussion

The synthesis of MoS<sub>2</sub> crystals is carried out in a CVD apparatus starting from MoO<sub>3</sub> and S powders and using PTAS and PTARG

as seeding promoters for the growth (see sketch in **Figure 1a** and **Figure S1** in the Supporting Information). On a large scale, the formation of the MoS<sub>2</sub> layers is inferred by means of micro-Raman investigations and XPS survey in areas of the sample with variable thickness. Two representative Raman spectra of the grown crystals are shown in **Figure 1b**. They present the distinctive in-plane, E<sub>2g</sub><sup>1</sup>, and out-of-plane, A<sub>1g</sub><sup>1</sup>, vibrational modes of MoS<sub>2</sub> located at frequency  $\omega(E_{2g}^1) \sim 381\text{--}383\text{ cm}^{-1}$  and  $\omega(A_{1g}^1) \sim 406\text{--}407\text{ cm}^{-1}$ .<sup>[17,18]</sup> The full-width half-maximum of the peaks is  $\Delta\omega \sim 4\text{ cm}^{-1}$  in both samples, a value comparable to that measured in geological sample, thus demonstrating the good crystallinity of the MoS<sub>2</sub> grown with the CVD approach.<sup>[17,18]</sup>

The high-resolution Mo 3d and S 2s photoemission peaks are shown in **Figure 1c** as a function of the binding energy (BE). The peak deconvolution, using pseudo Voigt functions, shows the presence of the Mo 3d<sub>5/2</sub> (at BE  $\sim 230.3\text{ eV}$ ), Mo 3d<sub>3/2</sub> (at BE  $\sim 233.4\text{ eV}$ ), and S 2s (at BE  $\sim 227.5\text{ eV}$ ) components in the two lines, respectively, both acquired on the PTAS- and PTARG-grown MoS<sub>2</sub> samples. Comparing the XPS components of the two samples, no chemical shift or shape modification can be observed, indicating that the MoS<sub>2</sub> nanosheets possess the same trigonal prismatic coordination typical of the 2H semiconductor phase and the same chemical constitution irrespective of the used seeding promoters.<sup>[19]</sup> Nevertheless, a first hint of the impact of the seeding promoter is observed at the valence band edge shown by the high-resolution XPS measurements in **Figure 1d,e**. Comparing the band edge of the synthesized materials with that of geological MoS<sub>2</sub> flakes, we observed that the highest occupied molecular orbital (HOMO) of the CVD MoS<sub>2</sub> is placed at  $\approx 1.42\text{ eV}$  binding energy for the layers obtained by using PTARG and  $\approx 1.47\text{ eV}$  using PTAS, thus resulting in a moderate shift toward the vacuum energy level (origin of the plot) compared to the HOMO energy at  $\approx 1.6\text{ eV}$  of the commercial MoS<sub>2</sub> flakes, inset in **Figure 1d**. Unequivocally, a modification of the electronic band structure occurs in the seeding promoter-assisted CVD MoS<sub>2</sub> layers.

As a first rationalization of the observed shift, we speculate that the perylene molecules not only promote the layered growth but also represent a reservoir of chemical groups able to functionalize the grown MoS<sub>2</sub> shifting the Fermi level. Moreover, comparing the band edges of the two types of CVD MoS<sub>2</sub>, we observe that the use of the PTARG molecule results in a broadening of the molecular core levels of the TMD (compare black and blue traces).

The local scale investigation of the material was performed by means of optical microscope (OM) inspection, scanning electron microscopy (SEM), and atomic force microscopy (AFM) analyses selecting individual monolayer MoS<sub>2</sub> domains. Both the representative OM and SEM images (**Figure 2a,b** and **Figure S2** in the Supporting Information) allow us to appreciate the formation of the MoS<sub>2</sub> layers on a large area ( $\approx \text{cm}^2$ ) of the samples. According to our statistics, we note that the size of the triangular monolayer domains is slightly larger when the PTAS seeding promoters is used, even though in both cases the lateral size well exceeds the tens of microns. The monolayer thickness, in the range of 0.7–1 nm, is confirmed by the linear AFM profiles shown in **Figure 2**.

The EFM investigation reveals a different electrostatic screening potential behavior in the monolayer domains obtained using the PTAS and PTARG molecules in **Figure 2c,d**,

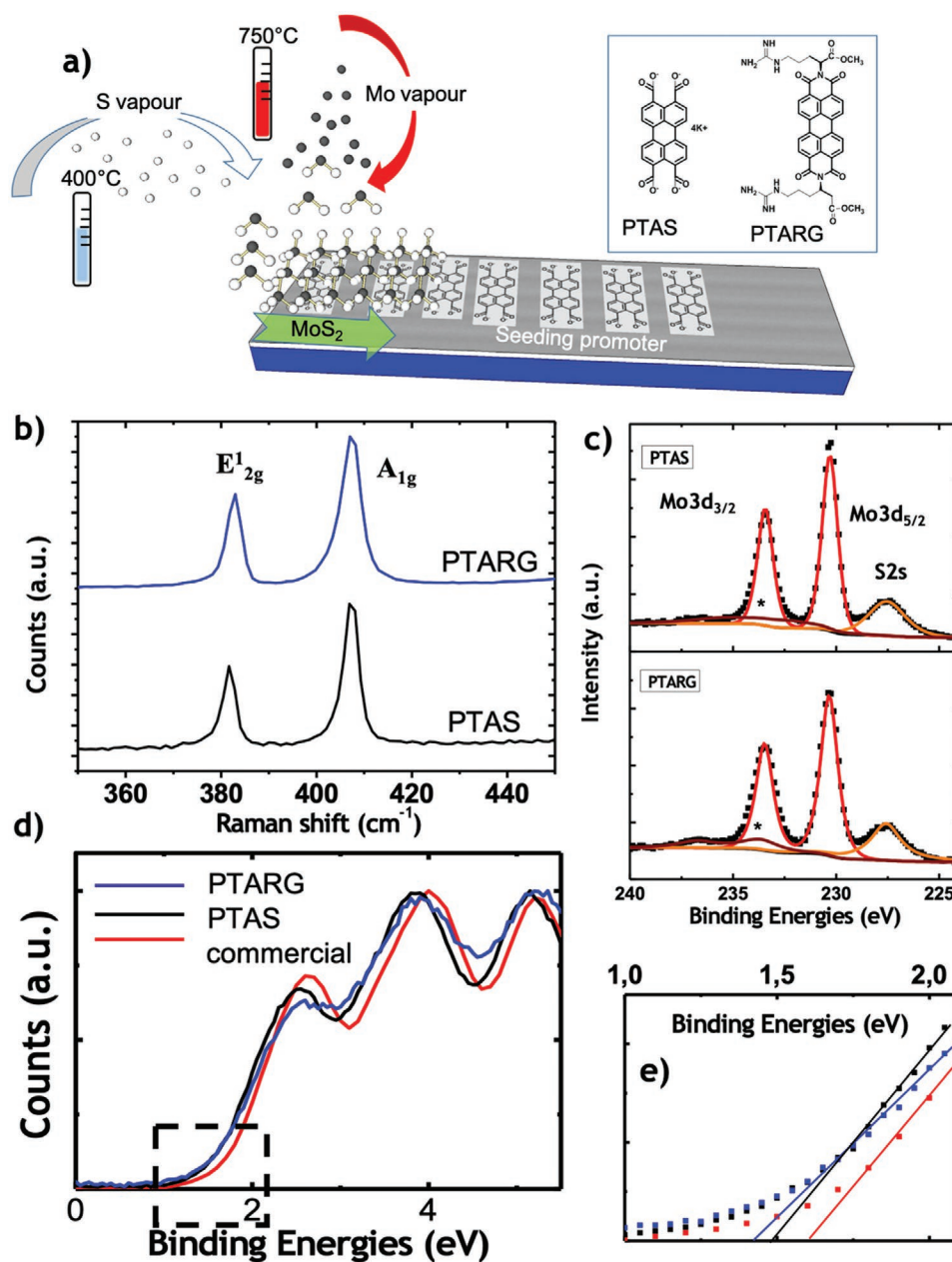


**Figure 1.** a) Sketch of the CVD process. The inset shows the chemical formula of the PTAS and PTARG seeding promoter. b) Raman spectra of the MoS<sub>2</sub> monolayer grown by using PTAS (black trace) and PTARG (blue trace). c) XPS analysis of the Mo 3d and S 2s core levels. Black squares are raw data, straight curves are fitted components. The negligible presence of oxide components is marked with “\*.” d) Valence band edge of the MoS<sub>2</sub> nanosheets grown on SiO<sub>2</sub> substrates using the two different seeding promoters and commercially available flakes. e) Zoom-in of the region delimited by the dashed box in panel (d).

respectively. The EFM investigations measure the shift of the resonance phase condition,  $\phi$ , caused by a variation of the electrostatic force between the sample and the conductive tip due to an applied bias voltage,  $V_g$ , see sketch in Figure 2e.<sup>[20–22]</sup> According to Equation (1) in the Experimental Section, the change in the slope of the function  $|\text{tg}(\phi)|$  versus  $V_g^2$  reveals that the capacitive coupling ( $C_1$ ) between the samples and the tip varies within the two MoS<sub>2</sub> monolayers.

To explain the data quantitatively, we calculated the capacitances called for in Equation (1), measuring the slopes of the

data in Figure 2e. Adopting the simplified model proposed in refs. [20,21], we calculated the capacitances  $C_1$  (SiO<sub>2</sub>)  $\approx 6.5 \times 10^{-19}$  F of the substrate (in quantitative agreement with refs. [20,21]), and  $C_1$  (MoS<sub>2</sub>)  $\approx 9.8 \times 10^{-19}$  F and  $\approx 10.6 \times 10^{-19}$  F of the MoS<sub>2</sub> monolayers obtained using PTAS and PTARG, respectively (see Equation (2) in the Experimental Section). The difference in the capacitances has a simplified description in terms of the electrical charges,  $Q'$ , induced at the AFM tip in response to the applied voltage bias,  $C_1 \sim V_g/Q'$ , see Figure 2e. These findings suggest that the amount of charges induced at

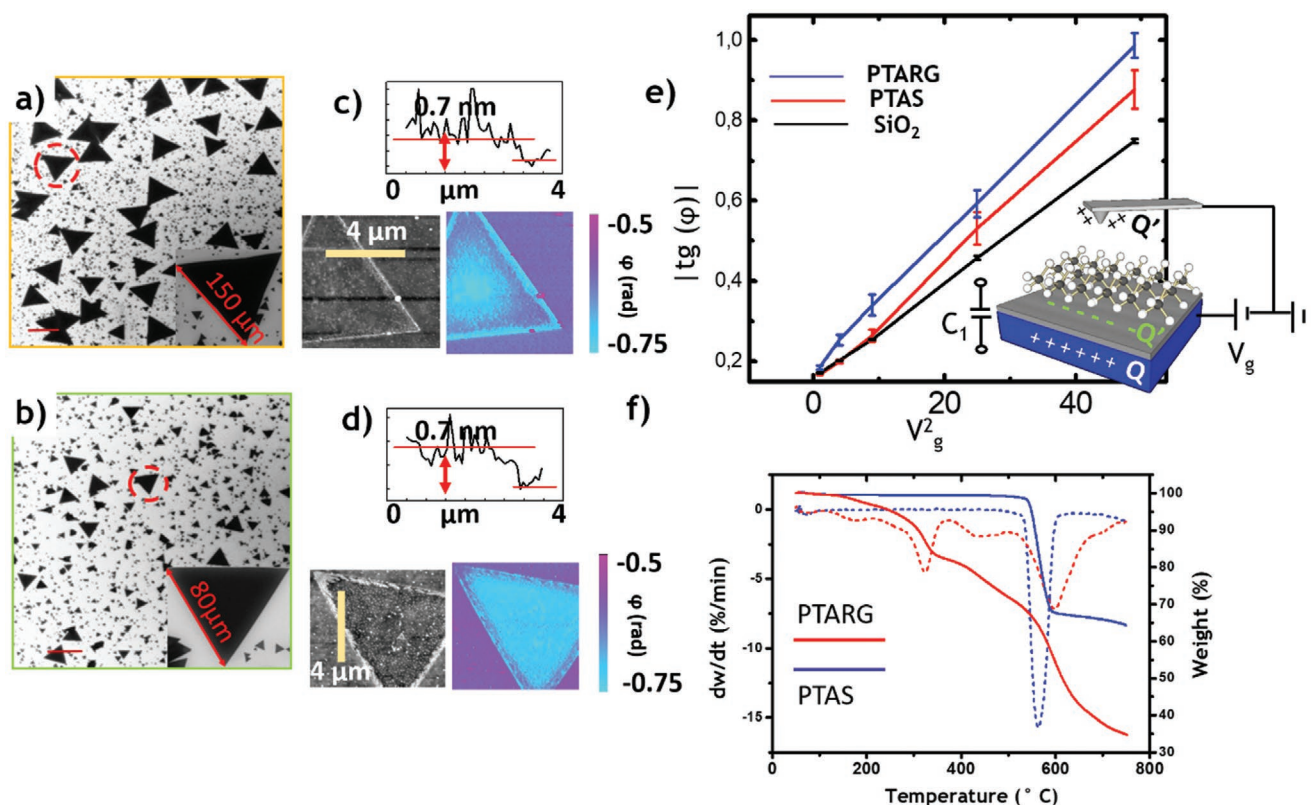


**Figure 2.** a,b) SEM images of the MoS<sub>2</sub> monolayers obtained by using PTAS and PTARG, respectively. c,d) Topographies and phase signals EFM images of the MoS<sub>2</sub> monolayers applying a gate voltage,  $V_g = 7$  V. The MoS<sub>2</sub> is obtained by using PTAS and PTARG, respectively. The insets show the height profile of the topography maps. e) Experimental configuration of the EFM measurements and plot of the  $|tg(\varphi)|$  function at different gate voltages for the bare SiO<sub>2</sub> substrate (black trace) and for the MoS<sub>2</sub> monolayer obtained by using PTAS (red trace) and PTARG (blue trace). f) TGA (full line) and DTG (dotted line) curves of PTAS (blue) and PTARG (red).

the tip, and screened by the presence of the MoS<sub>2</sub> monolayer, is reduced in the PTARG case compared to the PTAS one, thus showing an increase of the electrostatic screening potential at fixed biased voltage.

In EFM investigations of bulk materials, the variation of the screening potential efficiency is associated with a change of the local dielectric environment, which determines the capacitive tip-sample coupling.<sup>[23]</sup> In 2D materials, the confined nature of the atomically thin layer poses serious concerns on the physical definition of the dielectric constant, opening new room for the interpretation of the calculated capacitances, and thus of the screening potential efficiency, as a marker for the local polarizability of the electronic distribution and the presence of free charges trapped in the samples.<sup>[20–22,24]</sup>

At the atomic level, the main mechanism for the difference observed between the two monolayers can be related to extra free charges that are made available during the promoter degradation in the CVD process. We can speculate that this doping mechanism can follow different paths such as the inclusion of chemical functional groups in the MoS<sub>2</sub> lattice or the generation of lattice point defects, like vacancies, which are known to act as traps for free charge carriers and centers for localization of excitons.<sup>[25]</sup> To gain a deeper insight in the origin of this promoter-dependent electronic polarizability, we focused on the thermal stability of the seeding promoters during the CVD

growth performing TGA under inert atmosphere (Figure 2f). PTAS was found to be more thermally stable, because the initial decomposition temperature corresponding to 5% weight loss of PTAS was 540 °C, which is markedly higher than that of PTARG which initiates at 250 °C. The thermogram of PTAS showed a single weight loss in the temperature range 500–630 °C with a maximum rate at 561 °C, due to the loss of the carboxylic groups. Increasing the temperature up to 750 °C, the residue amount was ≈65 wt%, corresponding to the perylene core and the potassium ions. Under air exposure at 800 °C, the carbonaceous part of the residue is oxidized and remains a white residue ascribed to potassium oxide. The thermogram of PTARG is more complex due to the presence of many functional groups which are lost in various steps while the temperature is increasing. In this case, the TGA curve shows a broad degradation region between 100 and 750 °C. The derivative thermogravimetry (DTG) pattern, constituted by overlapping degradation events, indicates that various decomposition products are released in steps, with maxima at 177, 321, 432, 470, and 595 °C. Similar to PTAS, at the end of the thermal analysis, the residue (around 34%) is attributed to the perylene core; however, the carbonaceous residue disappears when exposed to air.

These experimental data show that at the working temperature of CVD (>650 °C) the only structure which remains unaltered is the perylene aromatic core, independently of the

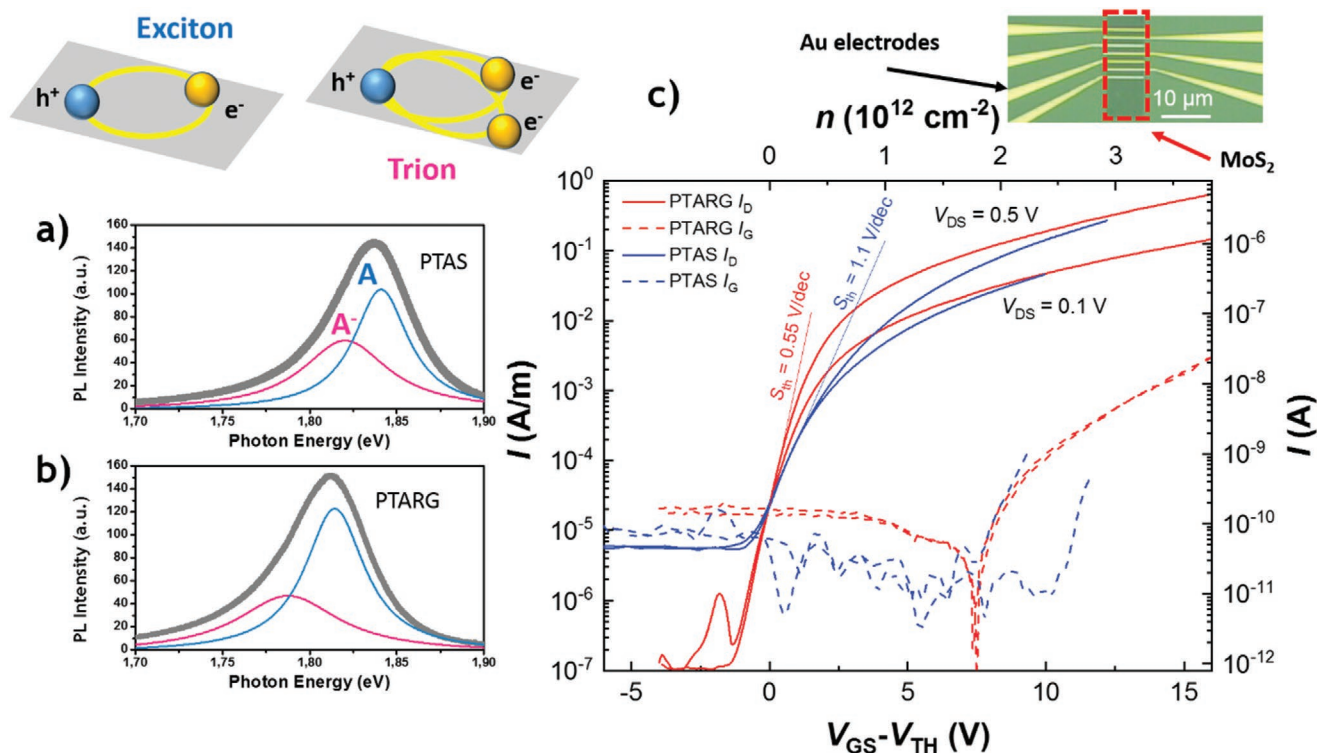


**Figure 3.** Sketch of the bound state of one hole and two electrons, also called trion. a,b) Micro-PL spectra of the triangular MoS<sub>2</sub> crystals shown in Figure 2c,d, respectively. The deconvolution of the spectra using Lorentzian components shows the contribution of the neutral A exciton and the charged A<sup>-</sup> trion. c) The transfer characteristics (the drain current  $I_D$  vs the back gate-source voltage overdrive  $V_{GS} - V_{TH}$ ) of the MoS<sub>2</sub> FETs in which the monolayer MoS<sub>2</sub> channel was grown by using the PTAS (blue lines) and PTARG (red lines) promoters. The characteristics are plotted for the drain-source voltages  $V_{DS}$  of 0.1 and 0.5 V. They are plotted as a function of  $V_{GS} - V_{TH}$  in order to compare the electrical properties of the FETs at the same carrier density  $n \propto V_{GS} - V_{TH}$ , which is also displayed in the plot (the as measured transfer characteristics are shown in Figure S3 in the Supporting Information). The FETs have relatively large subthreshold swing  $S_{th}$  (0.55 and 1.1 V dec<sup>-1</sup> for PTARG and PTAS-based FETs, respectively) due to the large thickness of the back-gate oxide (90 nm). We assumed that the threshold voltage of the FETs was reached at  $I_D/W = 23 \mu\text{A m}^{-1}$  (corresponding to  $I_D = 184 \text{ pA}$ ) because the drain currents  $I_D$  (solid lines) were comparable to the gate leakage currents  $I_G$  (dashed lines) for lower drain currents. The both types of FETs have a similar on/off ratio of  $\approx 3 \times 10^4$  in the range of the carrier density from 0 to  $\approx 4 \times 10^{12} \text{ cm}^{-2}$ . The inset shows an optical image of the PTAS MoS<sub>2</sub> FET.

starting seeding promoter. This result supports the morphological similarities observed in the MoS<sub>2</sub> grown using the two seeding promoters (Figure 2), while the different degradation of the functional groups, attached to the promoters, determines the discrepancy in the electrostatic screening potential as a result of the perturbation of the local electronic polarizability in the MoS<sub>2</sub> monolayer. The availability of extra charges, as responsible for the change of polarizability, can lead to a renormalization of the electronic band gap and the quasi-particle binding energy<sup>[26]</sup> along with a modification of the trion population and its weight in the radiative recombination.<sup>[13,27–29]</sup>

We elucidate these aspects by investigating the PL emission from MoS<sub>2</sub> monolayers as a function of the perylene promoters.<sup>[13,28,30]</sup> Figure 3a,b illustrates two representative PL spectra of the monolayer MoS<sub>2</sub> crystals obtained using the PTAS and PTARG seeding promoter, respectively. Each spectrum is fitted with two Lorentzian components that are assigned to the radiative recombination of the photoexcited quasi-particles. In agreement with previous reports on the optical transitions of MoS<sub>2</sub> monolayers,<sup>[28,31]</sup> they correspond to the neutral A exciton (the bound state of one hole (h<sup>+</sup>) and one electron (e<sup>-</sup>)) and the charged A<sup>-</sup> trions (the bound state of one hole (h<sup>+</sup>) and two

electrons (e<sup>-</sup>)). Averaging over a set of spectra acquired in ten different positions, we found that using the PTAS molecule the PL peaks are located at A<sup>-</sup>  $\sim 1.83 \pm 0.01 \text{ eV}$  and A  $\sim 1.85 \pm 0.01 \text{ eV}$ , while for the MoS<sub>2</sub> obtained from PTARG the energy positions of the peaks are A<sup>-</sup>  $\sim 1.79 \pm 0.01 \text{ eV}$  and A  $\sim 1.82 \pm 0.01 \text{ eV}$ . This fact indicates that, for both the exciton and the trion components, a shift toward lower energy ( $\Delta E \sim 30 \text{ meV}$ ) is observed in the MoS<sub>2</sub> monolayer grown with the PTARG seeding promoter. It is worth nothing that the shift is not negligible considering that, at room temperature, the exciton and trion binding energies for MoS<sub>2</sub> are 440 and 18 meV, respectively.<sup>[31,32]</sup> In terms of the relative trion and exciton weight, we note that the integral area ( $S$ ) of the components is  $S(A^-)/S(A) \sim 1.15 \pm 0.5$  for the PTAS and  $S(A^-)/S(A) \sim 0.9 \pm 0.4$  for the PTARG.

The variation of the PL spectra with the seeding promoter is consistent with the promoter-dependent electronic polarizability, which stems from extra charges available in the MoS<sub>2</sub> monolayer. In this respect, the higher activity of extra-charges should be reflected by a comparatively different in-plane transport characteristics of FETs made from different promoters. Indeed, it is reported that variation of the electrical conductance of the MoS<sub>2</sub> FETs can be caused by charges trapped in the

**Table 1.** Electrical characteristics of the FETs based on a monolayer MoS<sub>2</sub>.

	Threshold voltage $V_{TH}$ [V]	Extrinsic field-effect mobility $\mu_{FE}$ [cm <sup>2</sup> V <sup>-1</sup> s <sup>-1</sup> ]	On/off drain current ratio on/off
PTAS monolayer	-1.5 +/- 1.6	6	$3 \times 10^4$
PTARG monolayer	-7.8 +/- 2.1	6	$3 \times 10^4$

monolayer channel.<sup>[33,34]</sup> In particular, when extra-electrons are made available (e.g., due to oxygen or water molecules adsorbed on the channel), the threshold voltage ( $V_{TH}$ ) shifts toward positive gate voltages,<sup>[33]</sup> whereas it shifts toward negative voltages when those charges are lost. As such, the measurement of  $V_{TH}$  can be taken as a reference for a comparative study of the two monolayers obtained by using PTAS and PTARG.

Figure 3c (inset) shows an optical image of our device architecture. We investigated the electrical properties of a large array of FETs with channel length  $L \sim 1 \mu\text{m}$  and width  $W \sim 8 \mu\text{m}$ . In Figure 3c, we report on two representative transfer characteristics, i.e., the drain current ( $I_D$ ) versus the back gate-source voltage overdrive ( $V_{GS} - V_{TH}$ ) plots measured in our FETs. The FETs exhibit a typical n-type conduction behavior and a clear switching characteristic in both cases. Furthermore, the electrical properties of the FETs, summarized in **Table 1**, reveal that the threshold voltage,  $V_{TH}$ , is shifted toward more negative voltages in the case of the PTARG monolayer (the threshold voltages were obtained from the as measured transfer curves shown in Figure S3 in the Supporting Information). As stated before, these findings can be attributed to an increase of the MoS<sub>2</sub> channel electrical conductance due to the reduction of trapped electrons, which is in qualitative agreement with the EFM measurements and the reduction of the trion weight in the PL emission. PTARG monolayers also exhibit smaller subthreshold swing  $S_{th}$  of the transfer curves, which could be attributed to the lower density of charge traps at the interface between MoS<sub>2</sub> and SiO<sub>2</sub>.<sup>[35–38]</sup> At a given source–drain voltage,  $V_{DS}$ , the ratio between the drain current in the on state and the off state, on/off, does not vary significantly in the two cases and it is  $\approx 3 \times 10^4$ .

The extrinsic field-effect mobility,  $\mu_{FE} \sim 6 \text{ cm}^2 \text{ V}^{-1} \text{ s}^{-1}$  (see Equation (3) in the Experimental section) does not show a promoter-dependent variation as a function of the carrier density (see Figure S4 in the Supporting Information). We can explain this fact considering that, in its physical terms, the extrinsic field-effect mobility is dictated by the scattering events into the channel strictly related to the number of structural defects. From this point of view, the small variability observed in  $\mu_{FE}$  corroborates the structural similarity of the two MoS<sub>2</sub> monolayers derived from the XPS and micro-Raman analysis. Despite the absence of any post-fabrication thermal processing of our samples,  $\mu_{FE}$  (which includes the contact resistance) is comparable to that of CVD grown MoS<sub>2</sub> monolayers<sup>[39]</sup> and slightly lower than that of exfoliated geological MoS<sub>2</sub> crystals.<sup>[2]</sup>

### 3. Conclusion

In summary, we demonstrated that MoS<sub>2</sub> monolayers grown by CVD exhibit distinctive electronic polarizability when different

perylene-based molecules are used as seeding promoters. TGA on the molecules indicates that the thermal degradation of the seed molecules occurs differently with a single (PTAS) or multiple (PTARG) thermal events and the presence of various functional groups at CVD working temperatures affects the MoS<sub>2</sub> monolayer properties. We observed that the change of the local electronic polarizability, due to extra-charges trapped in the MoS<sub>2</sub> monolayers, leads to a modification of the PL emission peak, in terms of the spectral position and the relative exciton/trions radiative recombination. A back-gate FET architecture was used to test the in-plane electronic properties of the monolayer MoS<sub>2</sub> channel when shifting from one promoter to the other. Our results suggest that the modification of the electronic polarizability by perylene molecular promoter may represent a viable route to tailoring the opto-electronic properties of MoS<sub>2</sub> directly during the CVD growth and can provide a perspective for engineered doping inside a 2D monolayer.

### 4. Experimental Section

**Seeding Promoter Synthesis:** PTAS was prepared by the alkaline hydrolysis of 3,4,9,10-perylene tetracarboxylic dianhydride (Sigma Aldrich, CAS 128-69-8). Briefly, 3,4,9,10-perylene tetracarboxylic dianhydride (2.55 mmol) was added to 200 mL ethanol and stirred at reflux temperature for 30 min. After this period of time, while refluxing, 200 mL 3% KOH aqueous solution was dropwise added. The color was changed from a red suspension to a green solution. The reaction mixture was refluxed for an additional 12 h, then cooled at room temperature. After the reaction mixture was refluxed for 12 h and cooled to room temperature, ethyl ether was added to the solution until the product was precipitated. The precipitate was filtered and dissolved in deionized (DI) water and added in ethanol. The pure product was filtered and washed several times with ethanol.

**PTARG:** Perylene-3,4,9,10-tetracarboxylic dianhydride (1.3 mmol) was added to imidazole (29 mmol) at 110 °C under vigorous stirring. Arginine methyl ester dihydrochloride (1.8 mmol) was added to this mixture and intensively stirred for 4 h. The reaction mixture was cooled down when a dark red solid was precipitated. The precipitate was washed several times with methanol in order to eliminate the imidazole. A dark red solid was obtained in 75% yield (0.7 g). <sup>1</sup>H NMR (DMSO-*d*<sub>6</sub>): 8.25 (m, 4H), 7.90 (m, 4H), 4.33 (t, 1H), 4.11 (q, 2H), 3.21 (m, 2H), 1.95 (m, 2H), 1.69 (m, 2H), 1.20 (t, 3H).

**Growth of Seed-Assisted MoS<sub>2</sub>—Substrate Treatment and Preparation:** Before loading the SiO<sub>2</sub> (90 nm)/Si<sup>++</sup> substrates in the CVD apparatus, they were cleaned in isopropanol, acetone, and DI water, then dipped in a piranha solution for 2 h. After washing the substrates with DI water and drying by means of a nitrogen flux, a  $100 \times 10^{-6} \text{ M}$  solution of seeding promoter (in DI water) was repeatedly spread by drop casting on the SiO<sub>2</sub> placed on a hot plate (90 °C) for solvent evaporation.

**Material Growth:** MoS<sub>2</sub> crystals were grown on SiO<sub>2</sub> (90 nm)/Si<sup>++</sup> substrate in a CVD apparatus (planarTECH LLC) using a quartz tube as reaction chamber and two furnaces as upstream and downstream heating zones. In the upstream zone, 200 mg of sulfur powder (99.998%, Sigma-Aldrich) was loaded, while  $\approx 24 \text{ cm}$  away, in the downstream region, 1 mg of MoO<sub>3</sub> (99.98%, Sigma-Aldrich) was placed in a quartz boat. The substrate was placed directly on the top of the boat, facing the MoO<sub>3</sub> powder. Before starting the CVD process, the system was pumped down to a pressure of  $3 \times 10^{-4} \text{ mbar}$  and then purged with 1000 sccm high purity argon for several minutes. The two furnaces were heated up following the thermal ramps summarized in Figure S1 in the Supporting Information. The maximum temperature reached in the upstream furnace (sulfur region) was 300 °C and in the downstream furnace (MoO<sub>3</sub> region) was 750 °C. The high temperature step was lasted 25 min under the atmospheric pressure. The system was finally cooled

down to room temperature and 1000 sccm Ar flow was used to remove the reactants.

**Device Fabrication:** The MoS<sub>2</sub> FETs were fabricated directly on the growth SiO<sub>2</sub> (90 nm)/Si<sup>++</sup> substrates. The back of the substrates was used as a global back-gate. The MoS<sub>2</sub> FETs were patterned by electron-beam (e-beam) lithography using different types of poly(methyl methacrylate) resists. The MoS<sub>2</sub> channel (width  $W = 8 \mu\text{m}$ ) was defined by plasma etching using SF<sub>6</sub> (at a base pressure of 80 mbar, flow rate of 10 sccm, and power of 50 W) for 25 s. After defining the channel, the source and drain contacts (60 nm thick Au) were fabricated by evaporating Au in the e-beam evaporator at a base pressure of  $1.2 \times 10^{-6}$  mbar.

**Sample Characterization:** XPS measurements were performed on a PHI 5600 instrument equipped with a monochromatic Al K $\alpha$  x-ray source (energy = 1486.6 eV) and a concentric hemispherical analyzer. The spectra were collected at a take-off angle of 45° and band-pass energy of 23.50 eV. The instrument resolution was 0.5 eV. The spectra were aligned using C 1s (285 eV) as reference. Raman spectroscopy measurements were performed in a backscattering configuration employing a Renishaw InVia spectrometer, equipped with the 514 nm (2.41 eV) line of solid-state diode laser. The laser radiation was focused on the sample by means of a 50x Leica objective (0.75 numerical aperture), maintaining the incident laser power below 1 mW to avoid sample damage. The PL spectra were acquired in a Renishaw InVia spectrometer equipped with the 633 nm (1.96 eV) line of a HeNe laser. The laser radiation was focused on the sample by means of a 50x Leica objective (0.75 numerical aperture), maintaining the incident laser power below 1 mW to avoid sample damage. The AFM investigation of the samples was performed in tapping mode operating in an EFM configuration. The AFM-Bruker commercial system was equipped with conductive Pt/Ir-coated tips. The EFM measurements were carried out in a dual pass scan. In the first scan, the topography was acquired with the tip electrically grounded, in the second scan, the phase signal was acquired withdrawing the tip at a lift height of 30 nm above the surface and applying a DC electrical signal varied in the range 1–7 V. Note that the EFM maps were not affected by topographic artifacts being acquired in a second pass scan. In the EFM measurements, the phase shift due to the electrostatic force on the tip resulted<sup>[21]</sup>

$$|\tan\phi| = \frac{Q_f}{2k} C_1''(z) V_g^2 \quad (1)$$

where  $Q_f = 120$  and  $k = 2.8 \text{ N m}^{-1}$  are the quality factor and spring constant of the AFM cantilever, respectively, and  $C_1''$  is the spatial second derivative of the electrical capacitance between the substrate and the conductive AFM tip as a function of the lift height  $z$ .

Adopting the model proposed in refs. [20,21], the AFM tip was modeled as a parallel plate of radius  $R$  at a distance  $z$  above the SiO<sub>2</sub> dielectric layer of thickness  $t = 90 \text{ nm}$  and dielectric constant  $\epsilon_{\text{ox}} \sim 3.9$ . The model predicted

$$C_1(z) = \frac{1}{2} C_1''(z) \left( z + \frac{t}{\epsilon_{\text{ox}}} + \Delta \right)^2 \quad (2)$$

where  $\Delta = 0$  for the SiO<sub>2</sub> and  $\Delta = \frac{d}{\epsilon}$  with  $d = 0.7 \text{ nm}$  and  $\epsilon$ , respectively, the thickness and dielectric constant of the MoS<sub>2</sub> monolayer. Note that  $\Delta \ll \frac{t}{\epsilon_{\text{ox}}}$ , therefore this term was neglected in the calculation of the capacitances for the MoS<sub>2</sub> monolayers.

For the electrical characterization, all MoS<sub>2</sub> FETs were characterized by Keithley 2611A source-measure units in FormFactor EP6 and Summit 11000 probe stations in air ambient. The extrinsic field-effect mobility was calculated as

$$\mu_{\text{FE}} = \left( \frac{dI_D}{dV_{\text{GS}}} \right) \left( \frac{L}{W} \right) \left( \frac{t_{\text{ox}}}{\epsilon_{\text{ox}}} \right) \left( \frac{1}{V_{\text{DS}}} \right) \quad (3)$$

where  $t_{\text{ox}}$  is gate oxide thickness and  $\epsilon_{\text{ox}}$  is dielectric constant of the gate oxide.

TGA was performed on a PerkinElmer TGA-7 instrument under a nitrogen atmosphere. Before performing the TGA run, the sample ( $\approx 1 \text{ mg}$ )

was held at 50 °C for 30 min; the scan was carried out from 50 to 750 °C at a heating rate of 20 °C min<sup>-1</sup>. The residue of the TGA run was oxidized at 800 °C for 10 min under a 35 mL min<sup>-1</sup> flowing air atmosphere.

## Supporting Information

Supporting Information is available from the Wiley Online Library or from the author.

## Acknowledgements

Mario Alia is acknowledged for technical support. This research was partially funded by ACCORDO QUADRO Regione Lombardia project "I-ZEB" (decreto 7784/2016). This research was partially funded by the MIUR under the PRIN 2017 (aSTAR) grant 2017RKTWMTY. This research was partially supported by the EU H2020 Graphene Flagship Core 2 grant no. 785219. This work was also performed during the implementation of the project Building-up Centre for advanced materials application of the Slovak Academy of Sciences, ITMS project code 313021T081 supported by Research & Innovation Operational Program funded by the ERDF and was elaborated within the project VEGA 2/0161/17.

## Conflict of Interest

The authors declare no conflict of interest.

## Keywords

electronic polarizability, monolayer MoS<sub>2</sub>, perylene diimides, seeding promoters, thermogravimetric analysis

Received: May 6, 2020

Revised: July 27, 2020

Published online:

- [1] M. Chhowalla, H. S. Shin, G. Eda, L.-J. Li, K. P. Loh, H. Zhang, *Nat. Chem.* **2013**, *5*, 263.
- [2] B. Radisavljevic, A. Radenovic, J. Brivio, V. Giacometti, A. Kis, *Nat. Nanotechnol.* **2011**, *6*, 147.
- [3] S. Wachter, D. K. Polyushkin, O. Bethge, T. Mueller, *Nat. Commun.* **2017**, *8*, 14948.
- [4] F. H. L. Koppens, T. Mueller, P. Avouris, A. C. Ferrari, M. S. Vitiello, M. Polini, *Nat. Nanotechnol.* **2014**, *9*, 780.
- [5] G. Eda, S. A. Maier, *ACS Nano* **2013**, *7*, 5660.
- [6] J. D. Benck, T. R. Hellstern, J. Kibsgaard, P. Chakthranont, T. F. Jaramillo, *ACS Catal.* **2014**, *4*, 3957.
- [7] C. Martella, C. Mennucci, A. Lamperti, E. Cappelluti, F. B. de Mongeot, A. Molle, *Adv. Mater.* **2018**, *30*, 1705615.
- [8] Z. Cai, B. Liu, X. Zou, H.-M. Cheng, *Chem. Rev.* **2018**, *118*, 6091.
- [9] Y.-H. Lee, X.-Q. Zhang, W. Zhang, M.-T. Chang, C.-T. Lin, K.-D. Chang, Y.-C. Yu, J. T.-W. Wang, C.-S. Chang, L.-J. Li, T.-W. Lin, *Adv. Mater.* **2012**, *24*, 2320.
- [10] S. Vangelista, E. Cinquanta, C. Martella, M. Alia, M. Longo, A. Lamperti, R. Mantovan, F. B. Basset, F. Pezzoli, A. Molle, *Nanotechnology* **2016**, *27*, 175703.
- [11] X. Ling, Y.-H. Lee, Y. Lin, W. Fang, L. Yu, M. S. Dresselhaus, J. Kong, *Nano Lett.* **2014**, *14*, 464.
- [12] P. Yang, A. G. Yang, L. Chen, J. Chen, Y. Zhang, H. Wang, L. Hu, R. J. Zhang, R. Liu, X. P. Qu, Z. J. Qiu, C. Cong, *Nano Res.* **2019**, *12*, 823.

- [13] W. Su, H. Dou, D. Huo, N. Dai, L. Yang, *Chem. Phys. Lett.* **2015**, 635, 40.
- [14] Y. Xie, E. Wu, R. Hu, S. Qian, Z. Feng, X. Chen, H. Zhang, L. Xu, X. Hu, J. Liu, D. Zhang, *Nanoscale* **2018**, 10, 12436.
- [15] F. Zhou, J. Chen, X. Tao, X. Wang, Y. Chai, *Research* **2019**, 2019, 1.
- [16] P. S. Kollipara, J. Li, Y. Zheng, *Research* **2020**, 2020, 1.
- [17] C. Lee, H. Yan, L. E. Brus, T. F. Heinz, J. Hone, S. Ryu, *ACS Nano* **2010**, 4, 2695.
- [18] H. Li, Q. Zhang, C. C. R. Yap, B. K. Tay, T. H. T. Edwin, A. Olivier, D. Baillargeat, *Adv. Funct. Mater.* **2012**, 22, 1385.
- [19] H. Liu, K. K. Ansah Antwi, J. Ying, S. Chua, D. Chi, *Nanotechnology* **2014**, 25, 405702.
- [20] T. S. Jespersen, J. Nygård, *Nano Lett.* **2005**, 5, 1838.
- [21] C. Staii, A. T. Johnson, N. J. Pinto, *Nano Lett.* **2004**, 4, 859.
- [22] A. Castellanos-Gomez, E. Cappelluti, R. Roldán, N. Agraït, F. Guinea, G. Rubio-Bollinger, *Adv. Mater.* **2013**, 25, 899.
- [23] B. M. Law, F. Rieutord, *Phys. Rev. B: Condens. Matter Mater. Phys.* **2002**, 66, 354021.
- [24] T. Tian, D. Scullion, D. Hughes, L. H. Li, C.-J. Shih, J. Coleman, M. Chhowalla, E. J. G. Santos, *Nano Lett.* **2020**, 20, 841.
- [25] S. Tongay, J. Suh, C. Ataca, W. Fan, A. Luce, J. S. Kang, J. Liu, C. Ko, R. Raghunathanan, J. Zhou, F. Ogletree, J. Li, J. C. Grossman, J. Wu, *Sci. Rep.* **2013**, 3, 2657.
- [26] Y. Lin, X. Ling, L. Yu, S. Huang, A. L. Hsu, Y.-H. Lee, J. Kong, M. S. Dresselhaus, T. Palacios, *Nano Lett.* **2014**, 14, 5569.
- [27] S. Tongay, J. Zhou, C. Ataca, J. Liu, J. S. Kang, T. S. Matthews, L. You, J. Li, J. C. Grossman, J. Wu, *Nano Lett.* **2013**, 13, 2831.
- [28] S. Mouri, Y. Miyauchi, K. Matsuda, *Nano Lett.* **2013**, 13, 5944.
- [29] H. Nan, Z. Wang, W. Wang, Z. Liang, Y. Lu, Q. Chen, D. He, P. Tan, F. Miao, X. Wang, J. Wang, Z. Ni, *ACS Nano* **2014**, 8, 5738.
- [30] G. Eda, H. Yamaguchi, D. Voiry, T. Fujita, M. Chen, M. Chhowalla, *Nano Lett.* **2011**, 11, 5111.
- [31] K. F. Mak, K. He, C. Lee, G. H. Lee, J. Hone, T. F. Heinz, J. Shan, *Nat. Mater.* **2013**, 12, 207.
- [32] M. D. Tran, J. H. Kim, Y. H. Lee, *Curr. Appl. Phys.* **2016**, 16, 1159.
- [33] K. Cho, W. Park, J. Park, H. Jeong, J. Jang, T.-Y. Kim, W.-K. Hong, S. Hong, T. Lee, *ACS Nano* **2013**, 7, 7751.
- [34] W. S. Leong, Y. Li, X. Luo, C. T. Nai, S. Y. Quek, J. T. L. Thong, *Nanoscale* **2015**, 7, 10823.
- [35] Y. Y. Illarionov, A. G. Banskchikov, D. K. Polyushkin, S. Wachter, T. Knobloch, M. Thesberg, M. I. Vexler, M. Walth, M. Lanza, N. S. Sokolov, T. Mueller, T. Grasser, *2D Mater.* **2019**, 6, 045004.
- [36] C. Lee, S. Rathi, M. A. Khan, D. Lim, Y. Kim, S. J. Yun, D.-H. Youn, K. Watanabe, T. Taniguchi, G.-H. Kim, *Nanotechnology* **2018**, 29, 335202.
- [37] Y. Y. Illarionov, G. Rzepa, M. Walth, T. Knobloch, A. Grill, M. M. Furchi, T. Mueller, T. Grasser, *2D Mater.* **2016**, 3, 035004.
- [38] J. Xu, L. Chen, Y.-W. Dai, Q. Cao, Q.-Q. Sun, S.-J. Ding, H. Zhu, D. W. Zhang, *Sci. Adv.* **2017**, 3, e1602246.
- [39] K. A. Patel, R. W. Grady, K. K. H. Smithe, E. Pop, R. Sordan, *2D Mater.* **2020**, 7, 015018.